ORIGINAL PAPER

Damage Evolution of Coal with Inclusions Under Triaxial Compression

Yufeng Zhao[1] · Heinz Konietzky[1] · Martin Herbst[1]

Abstract
Along with the advance of the working face, coal experiences different loading stages. Laboratory tests and numerical simulations of fracture and damage evolution aim to better understand the structural stability of coal layers. Three-dimensional lab tests are performed and coal samples are reconstructed using X-ray computer tomography (CT) technique to get detailed information about damage and deformation state. Three-dimensional discrete element method (DEM)-based numerical models are generated. All models are calibrated against the results obtained from uniaxial compressive strength (UCS) tests and triaxial compression (TRX) tests performed in the laboratory. A new approach to simulate triaxial compression tests is established in this work with significant improved handling of the confinement to get realistic simulation results. Triaxial tests are simulated in 3D with the particle-based code PFC^{3D} using a newly developed flexible wall (FW) approach. This new numerical simulation approach is validated by comparison with laboratory tests on coal samples. This approach involves an updating of the applied force on each wall element based on the flexible nature of a rubber sleeve. With the new FW approach, the influence of the composition (matrix and inclusions) of the samples on the peak strength is verified. Force chain development and crack distributions are also affected by the spatial distribution of inclusions inside the sample. Fractures propagate through the samples easily at low confining pressures. On the contrary, at high confining pressure, only a few main fractures are generated with orientation towards the side surfaces. The evolution of the internal fracture network is investigated. The development of microcracks is quantified by considering loading, confinement, and structural character of the rock samples. The majority of fractures are initiated at the boundary between matrix and inclusions, and propagate along their boundaries. The internal structure, especially the distribution of inclusions has significant influence on strength, deformation, and damage pattern.

Keywords Coal sample · X-ray CT · Sample reconstruction · Triaxial compression test · Discrete element modeling · Flexible wall approach

List of symbols

C	Cohesion measured in laboratory [Pa]
$\bar{c}$	Cohesion assigned to bond in PFC^{3D} [Pa]
g_c	Contact gap interval assigned to bond in PFC^{3D} [m]
K^*	Normal to shear stiffness ratio assigned to bond in PFC^{3D} [–]
m	Mass of coal sample measured in laboratory [g]
N	Total number of particles in PFC^{3D} model [–]
r_p	Radius of particle in PFC^{3D} model [m]
V	Velocity (loading) assigned in PFC^{3D} [m/s]
V_{max}	Maximum velocity used for confinement in PFC^{3D} [m/s]
$\bar{\lambda}$	Radius multiplier assigned to bond in PFC^{3D} [–]
μ_c	Friction coefficient assigned to bond in PFC^{3D} [–]
ν	Poisson's ratio measured in laboratory [–]
ρ_p	Density of particle in PFC^{3D} model [kg/m^3]
σ_c	Uniaxial compressive strength (UCS) measured in laboratory [Pa]
σ_t	Tensile strength measured in laboratory [Pa]
$\bar{\sigma}_t$	Tensile strength assigned to bond in PFC^{3D} [Pa]
σ_3	Confining pressure [Pa]
Φ	Friction angle assigned to bond in PFC^{3D} [°

✉ Yufeng Zhao
 cnzhaoyufeng@hotmail.com

 Heinz Konietzky
 heinz.konietzky@ifgt.tu-freiberg.de

 Martin Herbst
 martin.herbst@ifgt.tu-freiberg.de

1 Geotechnical Institute, TU Bergakademie Freiberg, Freiberg, Germany

1 Introduction

Coal occupies the major portion in the energy resource structure of China (National Bureau of Statistics of China 2018). Therefore, a deeper understanding of the behavior of coal is a pre-requisite for effective and preferably environmental friendly usage of this resource. One of the aspects, which have to be considered is the fact, that distribution and mechanical behavior of cleats influence the mechanical behavior of coal, especially the failure pattern due to fracturing. Fracture characteristics (e.g. density, connectivity, and geometry) can be obtained by image analysis of core samples from the field (Wolf et al. 2004). Techniques developed for the sub-meter scale are adopted to measure cleat densities and spatial distribution using X-ray CT and image analysis (Mazumder et al. 2006; Wolf et al. 2008). X-ray CT became an effective non-destructive method for analyzing internal structures in rock materials, especially fractures in coal (Ketcham and Carlson 2001; Polak et al. 2003; Zhu et al. 2007; Karacan 2009; Karpyn et al. 2009; Kumar et al. 2011; Cnudde and Boone 2013; Pyrak-Nolte et al. 1997; Karacan and Okandan 2000; Van Geet et al. 2001; Mazumder et al. 2006; Wolf et al. 2008). Some studies (e.g. Verhelst et al. 1996; Simons et al. 1997; Van Geet et al. 2001) documented the feasibility in differentiating pores, fractures, and minerals in coal samples.

In addition to lab tests, numerical simulations of rock samples under triaxial loading are used to get deeper insight into the deformation and damage behavior. Models based on the particle method, which treat the rock as an assembly of bonded particles following the law of motion and considering the formation and interaction of micro-cracks at the grain-size level (e.g. Baumgarten and Konietzky 2012; Potyondy and Cundall 2004; Yan and Ji 2010) are promising. Zhao et al. (2009) performed some preliminary studies to investigate the sample deformation under different load configurations using the particle method (PM). A 3D implementation of a flexible membrane—necessary to perform triaxial simulations—generally requires a complex formulation or extensive computational power (Kuhn 1995; Uthus et al. 2008; O'Sullivan and Cui 2009). Many researchers simulated true triaxial tests, in which cubic samples were fixed within flat rigid boundaries (Sitharam et al. 2002; Belheine et al. 2009; Salot et al. 2009). Rigid boundaries are the most commonly used boundary condition for triaxial simulations of cylindrical samples and parallelepiped specimens (Belheine et al. 2009; Hasan and Alshibli 2010; Lu and Frost 2010). Other researchers simulated the effect of confining pressure by applying forces directly to the sample (Cheung and O'Sullivan 2008; Cui et al. 2008; O'Sullivan and Cui 2009; Wang and Tonon 2009). To properly reproduce the flexible latex membrane, a series of particles were generated to represent the membrane (particle membrane approach). The lateral stress conditions have been verified in detail by several researchers (Cheung and O'Sullivan 2008; de Bono et al. 2013). The main objective of this research is to develop a flexible membrane with independent wall elements for 3D conventional triaxial testing using PM. In contrast to a continuous rigid latex membrane and connected membrane particles, the new proposed membrane can stretch and shrink similar to a flexible membrane used during lab tests. The confining stress is uniformly applied to the side surface, and corresponding applied force on each wall element is calculated according to the target boundary condition. This approach guarantees that large and inhomogeneous deformation of the sample is reproduced in a correct manner for all phases of loading incl. the post-failure region.

2 CT Reconstruction

2.1 Sample Preparation

The tested coal samples are from the VI-15-14140 working face of Pingdingshan No. 8 Mine, China. Fresh rock pieces of coal were obtained directly from the underground mine. According to the drilling data, the average thickness of the coal seam located approximately 700 m below surface is 3.6 m. The average inclination angle of the seam is 22°. The density of the coal is 1.31 t/m^3. In total, 13 coal samples (marked as C1, C2, C3, C4, C5, C11, C12, C13, C15, C16, C21, C22, and C23) are collected and chosen to conduct different experiments. They are also used as basis for the numerical simulations. UCS tests and TRX tests are conducted in the laboratory and used for simulations. Samples C1, C2, C3, C4, and C5 are used for CT scanning, and sample C3 is scanned during an UCS test. The UCS tests of C3 and other three samples C21, C22, and C23 are used for numerical parameter calibration. TRX tests of C1, C2, C4, C5, C11, C12, C13, C15, and C16 are conducted in the laboratory. TRX tests are also simulated with reconstructed sample models C1–C5.

Cylindrical samples as shown in Fig. 1 were prepared with diameter of about 25 mm and length of about 50 mm following the ISRM Suggested Methods (Ulusay and Hudson 2012). Both ends were polished with parallelism of 2/100.

These core samples were first dried and then exact dimensions, density and porosity were determined (see Table 1) before CT scans were conducted.
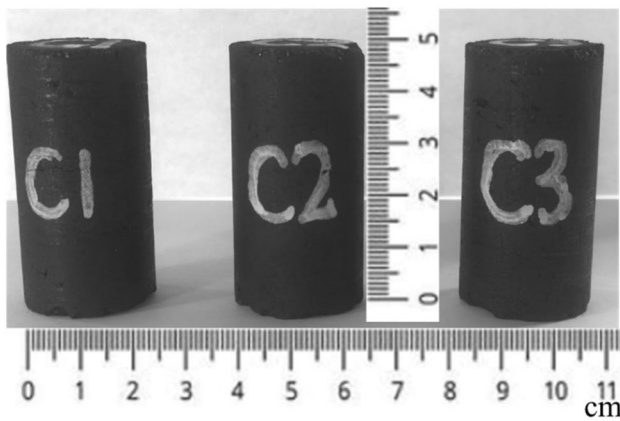
Fig. 1 Coal samples from underground mine Pingdingshan No. 8

2.2 CT-Based Reconstruction Procedure

CT scans were performed on an ACTIS-225FFI micro-xCT scanner as shown in Fig. 2a. The installation of a 225 kV Fein-Focus focal spot allows a minimum resolution of 10 μm for a cubic sample size of 4.8 mm. A charge-coupled device digital camera with a spatial resolution of 4.4 lp/mm (line pairs per mm) is used to capture and digitize the data of the Toshiba 3D image intensifier as detector system. The tested cylindrical core sample was placed in the sample couch and positioned in the center of the scanner's field of view. Under the applied conditions (180 kV, 200 μA at a raster of 750×750 pixels), the area of each pixel is approximately 50×50 μm^2. The scanning duration is 9 s per slice. Both, slice thickness and slice spacing were set to 50 μm. Figure 2b, c show the layout of the micro focus xCT device and the scanned slices of the sample.

Each CT scan produces a series of CT images (~ 1.010 slices for each scan). In total 10.100 images were produced from coal sample C3 for 10 different stages of uniaxial compression. The obtained images were used to reconstruct the 3-dimensional structure of the samples using digital image processing software. The attenuation data are transformed to CT numbers that have a range determined by the computer system (Yao et al. 2009). Theoretically, for a given X-ray energy, the CT number is a function of both, density and effective atomic number (Van Geet et al. 2001). CT numbers given in Hounsfield unit were exported as a collection of coordinates and values. The original file was processed by a program developed in MATLAB software (Solomon and Breckon 2011). Using this program, the CT numbers were transformed into grey scale values,

and the original files were transformed into 16-bit gray scale images.

By examining the images, a variety of errors and image artifacts are detected. The first author developed a program to detect these pixels. A nonlinear digital filtering technique (median filter technique) was used in MATLAB to remove the noise. Such noise reduction is a typical pre-processing step to improve the results of subsequent processing stages.

After transferring the original values into gray scale values, the segmentation technique defines an upper and a lower threshold of gray scale values for each component. Since CT values increase with density (and atomic number), they can be used to distinguish between mineral-filled and open fractures. Pre-existing and opened cracks have lowest gray values (white or nearly white). According to the different characters of coal matrix and mineral inclusions, proper gray scale value thresholds have been chosen to segment the image.

Materialise Mimics™, a software tool which is commonly used in medical research, was used to conduct the coal sample visualizations on the basis of the X-ray images (Rédei 2008). In Mimics™, the boundaries of each component are traced. All individual parts were assembled and the internal structure of the sample is reproduced. Exemplary, Fig. 3 illustrates the reconstruction process. Stl-format data files are generated to replicate different components.

The geometric structures of both—coal matrix and mineral inclusions—are generated via stl-files. The particles are re-grouped following these geometries. Five samples C1, C2, C3, C4 and C5, were generated according to the geometrical structure of real core samples. The internal structures incl. the different components are shown in Table 2 and Fig. 4. The amount of inclusions in samples C1 and C3 are obviously higher than those in samples C2, C4, and C5.

The inclusions, presented by red particles, have higher strength than the matrix. The inclusions in C1 (shown in Fig. 4a) are distributed mainly parallel to the axis of the sample. On the contrary, the inclusions in C4 and C5 (shown in Fig. 4d, e) are located isolated near the boundary surface in the central part and gathered at the top end, respectively. Especially in C4, both ends of the sample are composed of matrix particles, no large volume of inclusion is detected in this model.

Table 1 Average parameters of coal samples

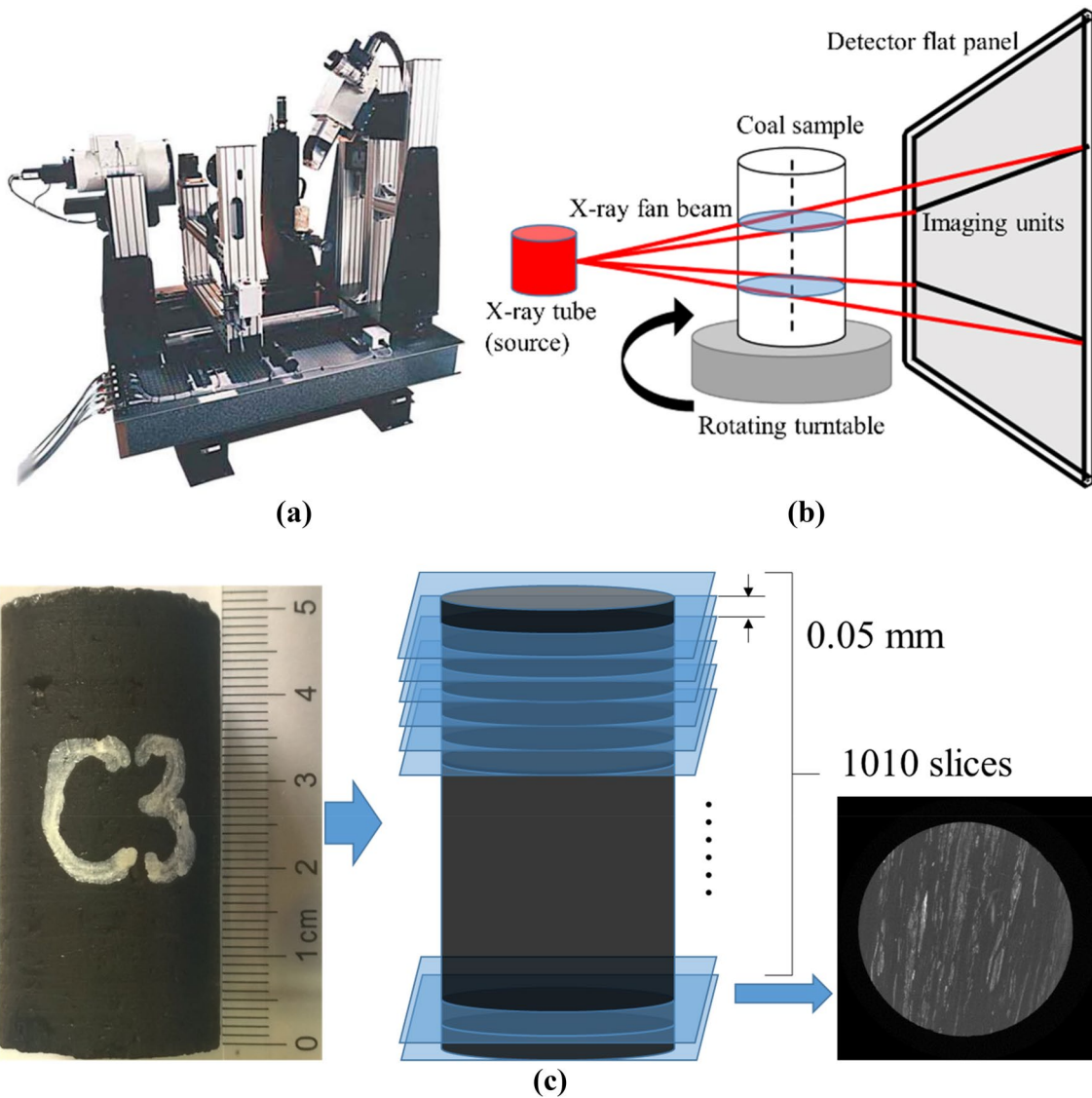|	Diameter D (mm)	Height H (mm)	Density ρ (g/cm^3)	Dry density ρ_d (g/cm^3)	Grain density ρ_g (g/cm^3)	Porosity φ (%)
Coal	25	50	1.30	1.30	1.39	6.5

Fig. 2 Micro-xCT scanner associated with rock testing system: **a** micro-xCT scanning device, **b** side view of schematic scanner layout, **c** illustration of complete scanning procedure
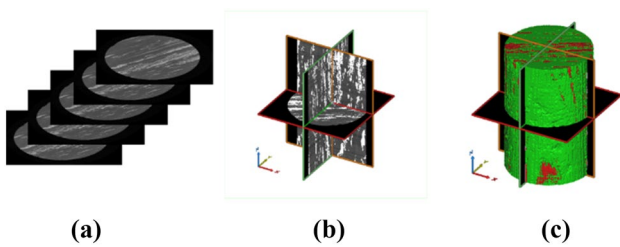

Fig. 3 3D model reconstruction based on 2D images: **a** stack of images, **b** cross sections in horizontal and vertical direction and **c** final 3D reconstruction

Table 2 Composition of coal samples

Sample no	Proportions	
	Matrix (%)	Inclusions (%)
C1	80.12	19.88
C2	86.06	13.94
C3	79.06	20.94
C4	89.90	10.10
C5	90.20	9.80
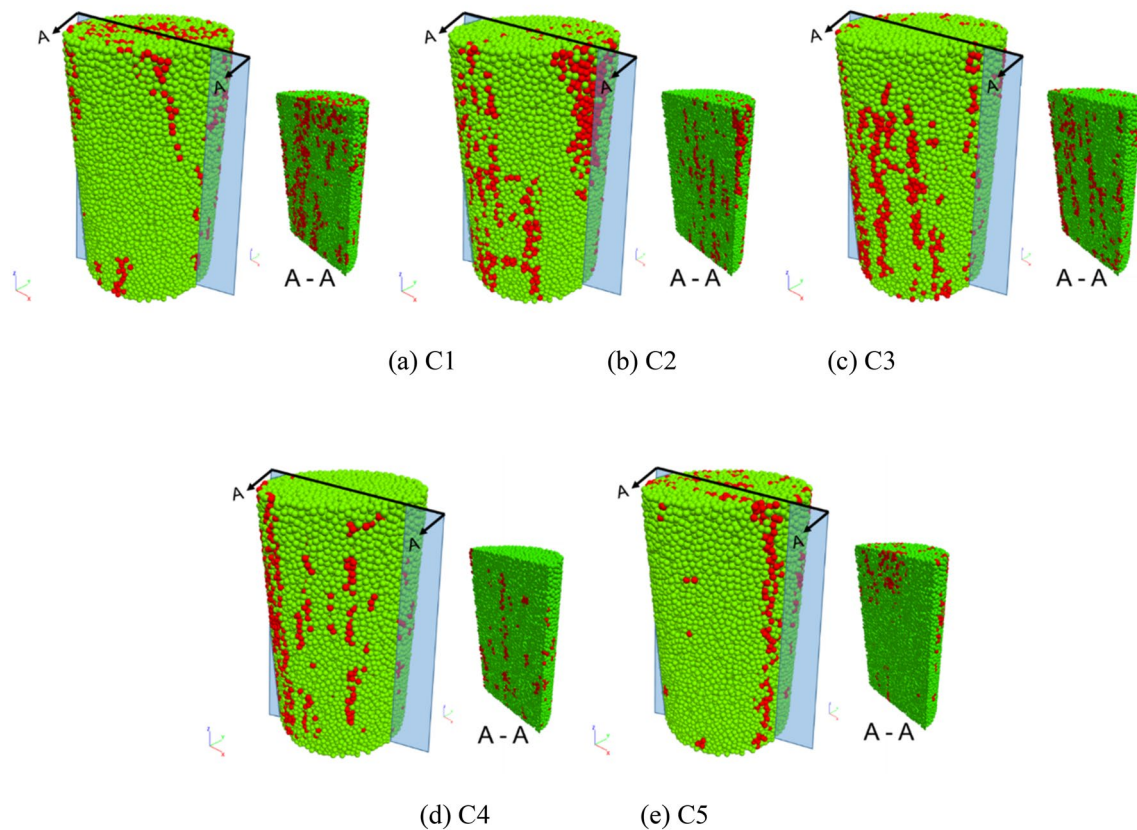
Fig. 4 Reconstructed numerical models of coal samples (green: coal matrix, red: inclusions) (Color figure online)

3 Triaxial Laboratory Experiments

3.1 Experimental Approach

A special triaxial pressure chamber (DBT A50-80-180 triaxial cell) was used for independent loading in radial and axial direction. The tests were conducted at room temperature of 20 ± 3 °C. The coal samples were not permitted to physically shrink or swell freely as a result of uniaxial strain, because they are under lateral confinement similar to in situ conditions. Hydraulic and mechanical pressures as well as strain and time were automatically monitored with sensors of high accuracy.

The cylindrical samples were wrapped by a polyvinyl chloride rubber core sleeve. The core sleeve provided optimal pressure transmission and maximum tightness during the entire test from low to maximum confining pressure. The samples are sealed even after failure. The sample material itself and the axial platens have been isolated from the confining fluid by the core sleeve. A stiff servo-controlled loading device is used to apply the loads. The maximum compressive force is 3600 kN. The high accuracy triaxial load cell was operated in a range from 0 to 1000 kN (calibration error is less than 0.05%; sensitivity is ± 0.5 kN).

The axial strain was measured by a linear variable displacement transducer (LVDT). The confining pressure is also servo-controlled. A maximum oil pressure of 80 MPa can be applied. The system is run by professional control software packages Test-Star-II Control System and Test-Ware from MTS. Together with the test system, an oil syringe pump was connected to the triaxial cell with a plug valve. The loading frame stiffness incl. the triaxial cell was first calibrated to obtain realistic deformations when samples are compressed.

Exemplary, sample C1 under 2.5 MPa confining pressure is used to describe the test procedure. After set-up and calibrating the test system, the servo-controlled program was activated to initialize the boundary conditions. Axial and confining pressures were raised to 2.5 MPa to reach a hydrostatic stress state. After the system has reached the hydrostatic state, axial load was applied by further movement of the upper loading plate. The axial load was applied with a very small speed of about 8×10^{-5} mm/s. The axial loading process was performed in steps: the loading process lasted every 750 s followed by a pause, the stress was kept constant for a period of time during the pause and was then further increased. This stepwise loading procedure was applied during the whole testing process.

Table 3 Physical parameters and test results of coal samples

Sample no	Confinement σ_3 (MPa)	Dimensions		Peak differential stress σ_P (MPa)	Final differential stress σ_R (MPa)
		D (mm)	H (mm)		
C1	2.5	25.50	50.60	25.94	16.44
C11	2.5	24.77	49.80	28.92	19.88
C13	5.0	24.99	50.02	41.44	26.91
C15	5.0	22.32	50.10	30.34	20.56
C4	7.5	25.47	50.85	44.45	34.31
C12	7.5	24.89	49.89	42.24	37.65
C16	7.5	24.54	50.28	46.83	32.18
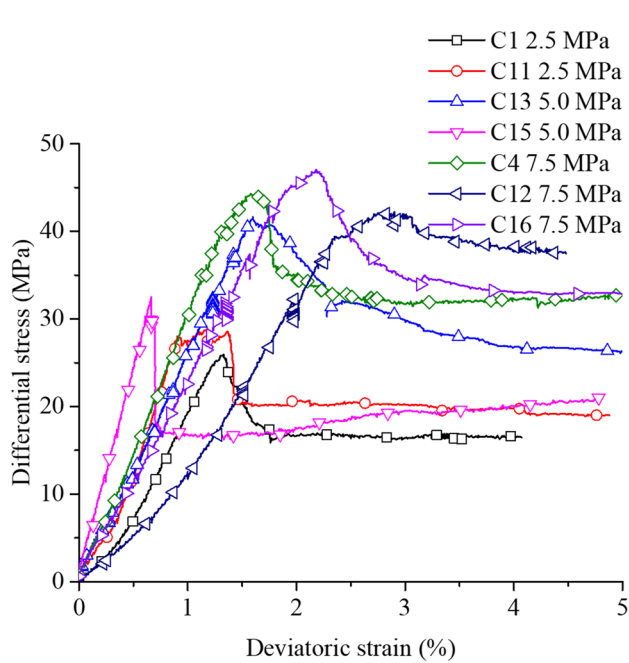
Fig. 5 Stress–strain curves of seven samples under triaxial compression

Fig. 6 Peak differential stress versus confining pressure

4 Results and Discussion

Seven coal samples with standard size were tested successfully in the laboratory with confining pressures of 2.5 MPa, 5.0 MPa and 7.5 MPa, respectively. Test results are shown in Table 3.

Peak differential stresses and corresponding strain values increase with increasing confining pressure. Corresponding stress–strain curves are shown in Fig. 5.

A linear fitting for peak differential stress as function of confining pressure results in Eq. 1 (see Fig. 6).

$$\sigma_p = 18.3432 + 3.5415 \cdot \sigma_3, \quad \left(R^2 = 0.8671\right) \tag{1}$$

in which, σ_p is peak differential stress (MPa), σ_3 is confining pressure (MPa).

The rubber sleeves were removed after testing and pictures were taken to observe the macroscopic fractures. After destruction, the fragments of four samples (C1, C13, C15, and C4) have been rebuilt with a digital processing method as shown in Fig. 7. The main structures of samples C11, C12, and C16 could not be retrieved, because of their severe deformation and destruction into many tiny fragments.

The fracture angle mentioned in this part represents the angle between main fracture surface and the horizontal plane. According to the reconstructed structures, fracture angles for different confining pressures were achieved as shown in Table 4. Under uniaxial loading, brittle coal samples were damaged mostly by vertical splitting, which means fracture angle was nearly 90°. The tested samples under triaxial compression showed shear failure, and fracture angles are between 50° and 80°. When the confining pressure was lower than 5 MPa, a single shear fracture appeared. The fracture angles decreased with higher confining pressure, and multiple parallel or intersected fractures appeared. With lower confining pressure, the fractures develop predominately along the vertical boundaries between matrix
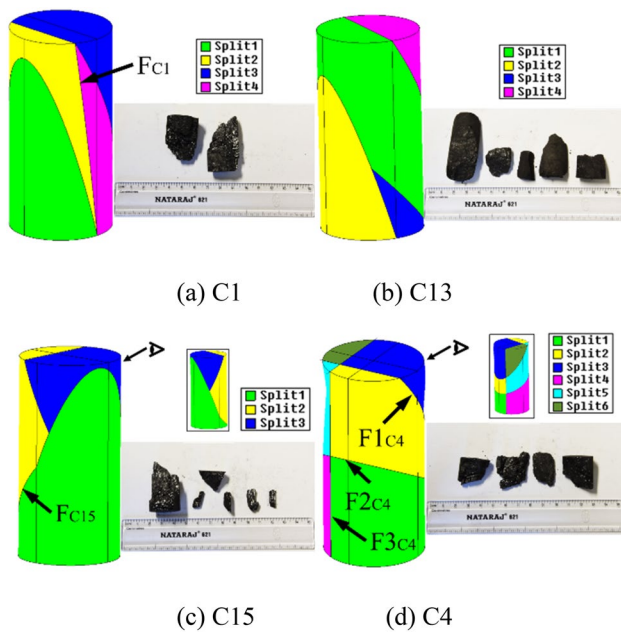
(a) C1   (b) C13

(c) C15   (d) C4

Fig. 7 Digital reconstructed structures of deformed (fractured) samples

and inclusions, but higher confining pressure prevent the vertical fractures from opening.

Fractures connecting top and bottom surfaces (final state of C1 and C15) cause a direct splitting of the samples. The vertical (or nearly vertical) main fractures in sample C1 and C15, marked as F_{C1} and F_{C15} in Fig. 7a, c, respectively, were generated in the early stage of compression. On the other hand, sample C4 also showed finally splitting, as shown in Fig. 7d, but fractures $F1_{C4}$ and $F2_{C4}$ were generated first, and the vertical fracture $F3_{C4}$ occurred in a later stage. All the fragments of sample C4 were compacted and extremely tight when $F3_{C4}$ was formed.

5 Numerical Simulation of Triaxial Compression Test

5.1 Novel Approach to Simulate Confinement

A new modelling procedure for conventional triaxial tests using PM based modelling approaches (called 'flexible wall approach' = FW approach') is proposed. It includes two steps:

(1) The first step comprises the sample generation. The reconstructed 3D models (see Sect. 2.2 section) are transformed into 3D numerical models (Zhao et al. 2010). For this study, the PM code PFC^{3D} (Itasca 2008) is chosen. The model is assigned with linear parallel bonds including appropriate parameters. At bottom and top of the sample horizontal walls are installed to apply the vertical load. The numerical simulations are performed in a strain-controlled mode by specifying constant velocities at the top and bottom walls. The simulations are conducted in a quasi-static mode. Spherical observation regions are installed inside the model to verify the stress conditions. Only a small friction coefficient of 0.1 was assigned to the interfaces between wall and top and bottom of the sample. This friction coefficient is useful to prevent sliding and rotation of the numerical model (potential problem of numerical instability), but it also duplicates the real test conditions in the lab.

(2) The second step considers the confinement. A lot of small wall elements are distributed around the sample to provide the confining stress. The flexible rubber membrane is duplicated by a set of isolated wall elements (new procedure), instead of one piece of cylindrical wall (classical approach).

The spatial position of each wall element is determined by sets of functions. In the parameter assignment file, the number of square wall units along the circumference is defined with a certain value (for instance 16 for demonstration model). Circular arranged wall elements are

Table 4 Fracture parameters of different coal samples after final destruction

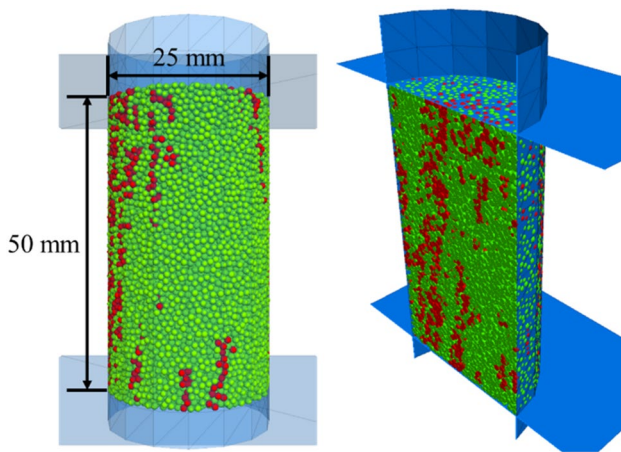| Sample No	C1	C13	C15	C4
σ_3 (MPa)	2.5	5.0	5.0	7.5
Main fracture angle θ_f (°)	75	73	68	52
Surface area A_{all} (mm^2)	917.00	904.30	1079.82	637.84
Verbal description	One main fracture with parallel fractures	Parallel fractures crossed by another fracture	V-shaped fractures	Multiple fractures with one vertical fracture

Fig. 8 Reconstructed PM sample with FW membrane as outer vertical boundary

stacked together vertically to cover the entire sample as the membrane. The coal sample C1 is taken as example. The cylindrical membrane is longer than the sample to fully cover the model under any kind of deformation. Sample model and wall elements are shown in Fig. 8, the red and green particles represent mineral inclusions and coal matrix, respectively. To simulate the confinement, wall servo commands are applied to each wall element to guarantee the desired stress. For example, with a calculated wall area of 11.52 mm^2, an initial target force of 30.21 N is applied on each triangle wall element to maintain 2.5 MPa confinement.

Tests were performed with confining pressures of 2.5 MPa, 5.0 MPa and 7.5 MPa, respectively. For each wall element, the target force is calculated by the defined confining pressure multiplied by its actual area. The simulated hydraulic pressure acts on the normal direction of the wall elements. The coordinates of the vertices are permanently recorded during the simulation, which is essential for updating the confinement (position of wall corners and forces). First, the desired hydrostatic state of stress is simulated followed by increasing vertical load at constant

confinement. The simulations were run until the residual stress value drops to 60% of the peak stress in the post-failure region.

During the test, the model sample deforms continuously and the side surfaces become uneven due to the inhomogeneous lateral strain induced by damage evolution. In this model, each wall element representing the membrane is isolated, and the dynamic state of a wall element is only determined by the wall-servo function. Deviations from the target force lead to a translational velocity on the wall elements to achieve the desired condition. Consequently, nearly constant target stresses are maintained by the movement of the wall elements.

Figure 9 illustrates the updating process for the wall elements representing the sleeve. Wall 1 and 2 consist of isosceles rectangular triangles as shown in Fig. 9b. Wall elements 3, 4 and 5 are the lower left triangles from the right unit, upper unit and diagonal/opposite unit, respectively. Point B, C and D are the lower left vertices of wall elements 3, 4 and 5, respectively. After several steps, the wall elements move to new positions as shown in Fig. 9c and the triangles 1 and 2 are stretched and become triangles 1′ and 2′ with the new vertices B′, C′ and D′. All the wall elements are adjusted according to the same rule, so that the confining structure is kept continuously updated to duplicate the deformed membrane.

When a wall is updated to a new shape, the wall area also changes because of the deformation. Constant target force is no longer correct for the new situation. According to the applied function, the area of each wall unit is calculated again after stretching or squeezing, and a new target force (equivalent to the confining pressure) is applied. By running these functions, the overall confinement remains constant even if significant deformations occur.

The parameters of the wall-servo function affect the results, because the target forces on each wall element are updated automatically. Therefore, the maximum velocity of the wall units should be slightly larger than the loading velocity. The applied velocity of the servo walls has great influence on simulation results. Its effect can be summarized

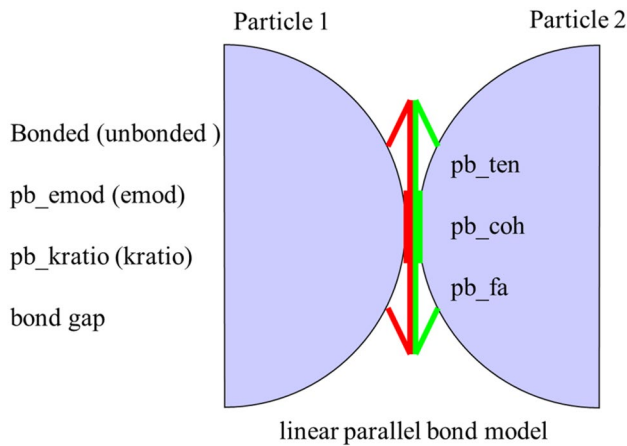**Fig. 9** Sketch to illustrate the wall element updating process (FW approach)
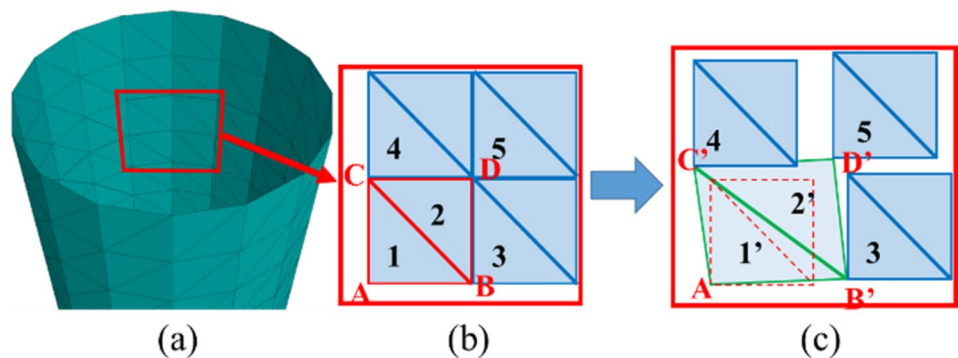
Fig. 10 Components and parameters of the linear parallel bond model (Potyondy and Cundall 2004)
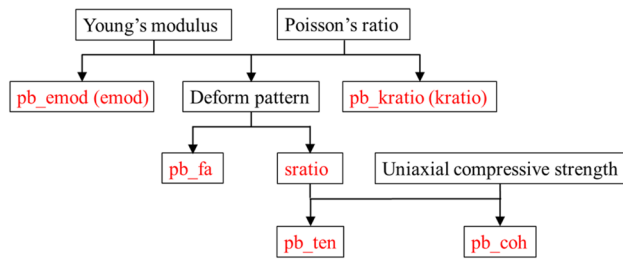

Fig. 11 Sketch to illustrate the calibration of the micro parameters

as follows: the moving of wall elements may not be able to follow the deformation of the model with small velocity; but if the maximum velocity is much higher, unrealistic displacements may happen, so either huge ball or ball/wall overlaps may occur, which can cause unrealistic deformation of wall elements.

5.2 Calibration and Verification

As shown in Fig. 10, a linear parallel bond model, which considers elastic normal and shear stiffness as well as cohesion, tensile strength and friction, is used in this work to simulate the coal sample.

Within the calibration process, the micro mechanical parameters of the contacts between the particles (see Fig. 11) such as bond elastic modulus (*pb_emod*), normal to shear stiffness ratio (*kratio*), tensile and shear strength as well as friction angle (*pb_fa*) were considered. Some parameters have cross effects with each other on the macroscopic parameters, such as Poisson's ratio, peak strength and failure pattern.

Three cylindrical samples with diameter of 25 mm and length of 50 mm were selected for the calibration process. Lab test results from UCS tests (see Table 5) are used as reference.

According to experience, parallel bond effective modulus (*pb_emod*) and elastic modulus follow a linear relationship. The ratio of normal to shear stiffness (*kratio*) and the macroscopic Poisson's ratio show a logarithmic relationship in the elastic stage. The ratio of tensile strength to cohesion (*sratio*) influences the deformation pattern. When *sratio* is fixed, the macroscopic strength changes linearly with the values of tensile and shear strength. Friction angle (*pb_fa*) has no effect before simulated samples reach peak strength, but it affects the ratio of tensile to shear cracks (*cratio*). These rules are considered for the calibration process. The following steps are performed to calibrate the mechanical parameters:

(1) The linear group elastic modulus (*emod*) is analyzed. A default linear model is assigned to all elements when generating the model. Then it is replaced by a parallel bond model between particles during the bonding phase. The linear group type is activated again after failure of the parallel bond group.

(2) The contribution of *pb_emod* to the macroscopic compression modulus is investigated. Different *pb_emod* and *emod* are introduced within predefined intervals, and all other parameters are set to relatively high values, so that finally the requested values for *emod* and *pb_emod* are found.

(3) *kratio* and macroscopic Poisson's ratio are determined for fixed values of *emod* and *pb_emod*. *kratio* and *pb_kratio* are assumed to be identical. Uniaxial compression simulations are performed with different *pb_kratio*. Poisson's ratios at different axial strains are calculated for each model, so that finally *kratio* and *pb_kratio* are obtained.

(4) *sratio* is investigated. The particle bonds are assigned by *pb_emod*, *pb_kratio*, tensile strength (*pb_ten*), cohesion (*pb_coh*) and friction angle (*pb_fa*). The shear

Table 5 Physical and mechanical parameters of coal samples obtained from UCS tests

Sample no	H (mm)	D (mm)	m (g)	ρ (g/cm^3)	σ_c (MPa)	E (GPa)	ν
C21	50.60	25.50	37.20	1.44	16.28	2.73	0.37
C22	50.80	25.53	37.28	1.43	13.08	2.21	0.34
C23	50.86	25.50	37.57	1.45	15.55	2.17	0.35
Average	50.75	25.51	37.35	1.44	14.97	2.37	0.35

bond strength is not modifiable directly in the simulation, but is set via *pb_ten* and *pb_coh*. A series of simulations are performed with fixed strength ratios. Finally, *sratio* and *pb_fa* are determined, also based on crack distribution and behavior in the post-peak stage.

(5) A reference tensile strength is defined as well as a factor relating microscopic tensile to compressive strength parameters. The factor is chosen in such a way that it fits the macroscopic ratio observed in the lab.

(6) In the last step, the parameters are slightly modified according to the real simulation conditions. The parameters of the inclusions (kaolinite) are also calibrated by the same method according to the mechanical properties given in literature (Randall et al. 2009; Zhao et al. 2010; Mahabadi et al. 2012). The measured physical and mechanical parameters of the matrix (coal) and the inclusions (kaolinite) are shown in Table 6.

The stress–strain curve of the calibrated numerical model for an UCS test is shown in Fig. 12 in comparison to lab test results.

The verified parameters are also valid for triaxial compression tests. Parallel-bond contacts are assigned to coal matrix, mineral inclusions and at the interface. By conducting minor adjustments, final parameters are obtained for triaxial testing as shown in Table 7.

Exemplary, triaxial simulation results of sample C1 are shown in Fig. 13 for a confining pressure of 2.5 MPa. Formed fracture networks in each stage are also shown (shear and tensile cracks are represented by red and green disks, respectively). Differential stress is the difference between axial stress and confining stress. The deformed membrane is plotted as a continuous set of wall elements.

According to equilibrium requirements, average vertical and horizontal stresses inside the sample should be consistent with applied boundary conditions. This criterion is used to verify the simulation results. The final deformed state of the reconstructed sample C1 under 2.5 MPa confining pressure is shown in Fig. 14. The triaxial compression simulation of model with FW approach shows significant uneven bulge. The isolated flexible wall elements have obvious advantages compared with rigid walls.
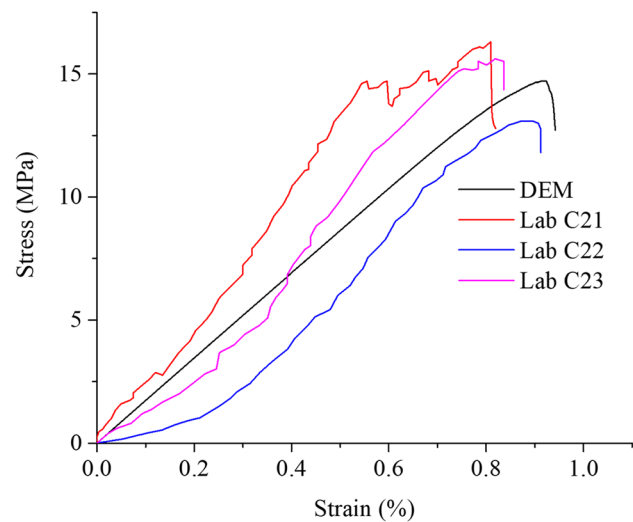

Fig. 12 Uniaxial compression tests: lab tests vs numerical model results after calibration

6 Numerical Simulation Results and Discussions

Figures 15, 16 and 17 show the stress–strain behavior obtained from 3-dimensional triaxial numerical simulations using the FW approach in comparison with the corresponding laboratory tests for confining pressures of 2.5 MPa, 5 MPa and 7.5 MPa, respectively. In general, good agreement has been achieved between numerical simulations and laboratory experiments. The differential stress reaches a constant value in the post-failure region until the end of the simulations. The initial slope in the elastic stage and the trend of residual strength observed during laboratory tests are well reproduced by the numerical model using the FW approach.

Meanwhile, a model with particle membrane approach is also simulated for comparison. The result of this traditional method is plotted in Fig. 15 (presented by light blue curve). Same parameters were assigned to the model, and the observed strength is significantly lower than using the FW approach. With the particle membrane, the force applied on each ball is constant during the simulation. The deformation of the sample cannot be transmitted to proper updated boundary conditions. Therefore, this method has

Table 6 Physical and mechanical parameters of coal sample (Zhao et al. 2010)	Groups	ρ (g/cm³)	E (GPa)	ν	σ_t (MPa)	C (MPa)	Residual cohesion C_{res} (MPa)	Initial friction angle θ (°)	Residual friction angle θ_{res} (°)
	Matrix	1.3	2.37	0.35	0.23	1.13	0.11	35	30
	Inclusion	1.8	16	0.18	1.11	6.45	–	34.6	–

Table 7 Micro-mechanical parameters of the numerical coal model

Element	Parameter	Coal matrix	Mineral inclusion	Boundary between matrix and inclusion
Particles	N	27,390	7218	–
	r_p (mm)	0.5	0.5	–
	ρ_p (kg/m³)	1390	1810	–
Contacts	$\bar{\lambda}$	1	1	1
	E (GPa)	2.09	2.84	1.90
	K^*	14.65	2.44	1
	$\bar{\sigma}_c$ (MPa)	17.40	30.50	11.60
	$\bar{c}$ (MPa)	4.35	12.20	5.8
	μ_c	0.4	0.4	0.4
	Φ (°)	4	7	8
	g_c (mm)	0.05	0.05	0.05
Axial loading control				
Walls	v (m/s)	0.005		
Confinement control				
Walls	Maximum velocity v_{max} (m/s)	0.01		

Fig. 13 Simulated stress–strain curves and crack evolution for coal sample C1 with 2.5 MPa confining pressure using the FW approach
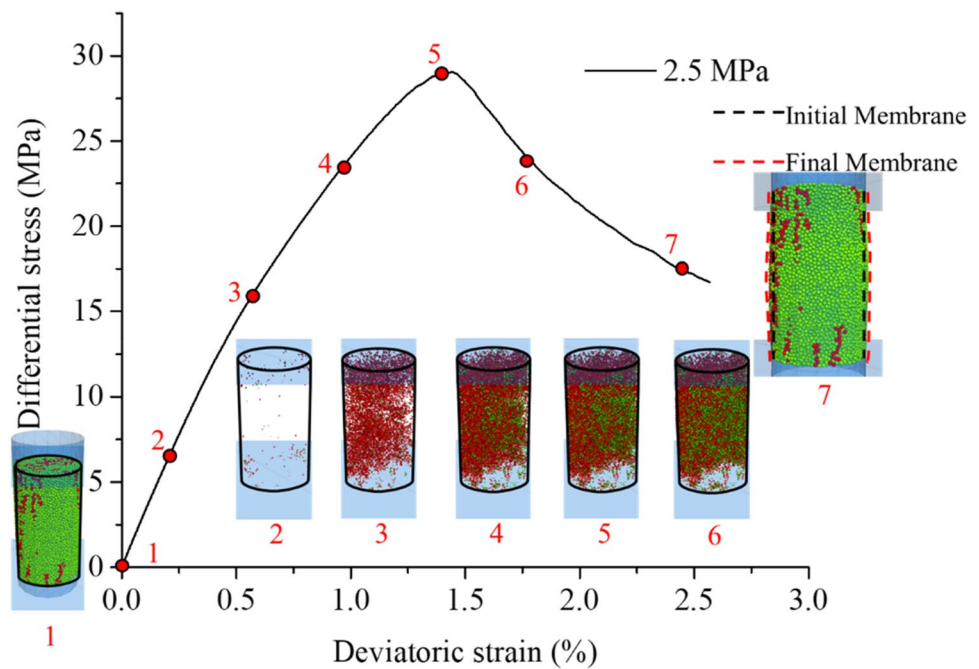
some significant limitations. On the other hand, the model with FW approach is able to follow the actual sample deformations.

Because of the distinct different amount of inclusions, the stress–strain behavior also shows great differences. Samples C1 and C3 have similar amount of inclusions (about 20%), but samples C2, C4 and C5 have only 10% as mentioned in Table 2. Samples with larger amount of inclusions like C1 and C3 show higher peak strength compared with other samples under the same boundary conditions. This

results proved that, compared with proportion of inclusions, the structural features have a decisive influence on the strength. Vertical aligned inclusions in model C1 and C3 (see Fig. 4a, c) provide more resistance against uniaxial loading. At lower confining pressure as 2.5 MPa, this difference between peak differential stresses $\Delta\sigma_P$ becomes less pronounced (see Fig. 15), the difference between C1 and C4 is 1.79 MPa. When the confining pressure is 5.0 MPa, the difference is 3.05 MPa. With high confining pressure, for example 7.5 MPa (see Fig. 17), splitting is restrained, the
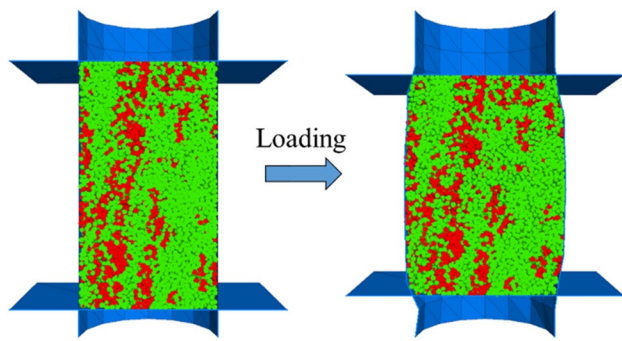
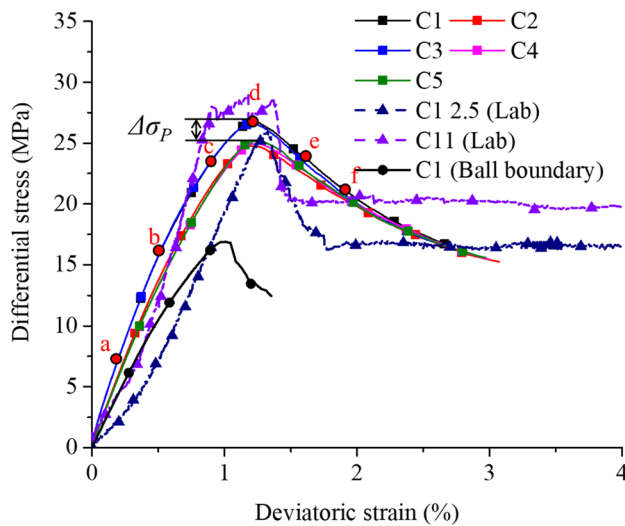**Fig. 14** Cross section of model C1 with FW approach before and after simulation

Fig. 15 Stress–strain curves of numerical simulations and laboratory tests with 2.5 MPa confining pressure
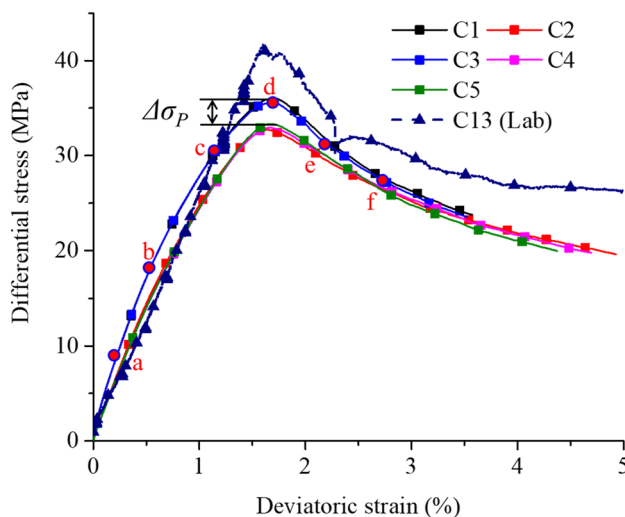

Fig. 16 Stress–strain curves of numerical simulations and laboratory tests with 5.0 MPa confining pressure
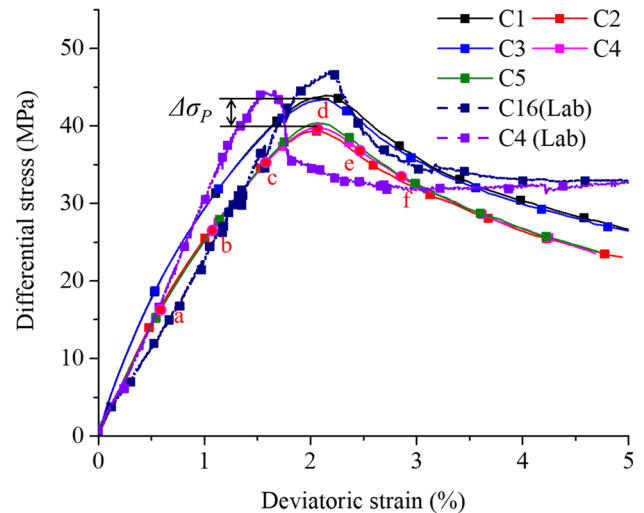

Fig. 17 Stress–strain curves of numerical simulations and laboratory tests with 7.5 MPa confining pressure

support of vertically distributed inclusions is more remarkable and the difference between peak differential stresses of C1 and C4 increases to 4.09 MPa.

Differential stress and number of triggered microcracks have been recorded as well as the evolution of internal force chains. These results provide insights from the microscopic perspective. Not only the heterogeneity in mineral composition, but also the distributions of inclusions and contacts between grains have influence on crack initiation and propagation.

The force chains and crack distributions inside the models C1, C3, and C4 at different confining pressures are shown in Figs. 18, 19 and 20. Short straight lines represent the contact forces by connecting the centers of two touching particles or forces at the particle–wall element contacts. The force networks are scaled by contact force magnitude. The line thickness is directly proportional to the magnitude. On the other hand, internal stress redistributions lead to initiation and propagation of cracks as also shown in Figs. 18, 19, and 20. Crack elements are plotted as cubes in 3-dimensional plots and boxes in 2-dimensional cross sections to identify their positions and area of influence. By investigating the evolution of cracks during the simulations, information about internal damage evolution can be obtained. Shear and tensile cracks are marked by red and green boxes, respectively. The crack propagation during triaxial test simulations evolves with increasing uniaxial strain. The plots indicate that denser crack networks are initiated in the central region vertically before failure. After failure, the crack network shows column-like distribution at lower confinement as shown in Fig. 18e; while the cracks tend to concentrate near the center of the sample at high confinement as shown in Fig. 20e.
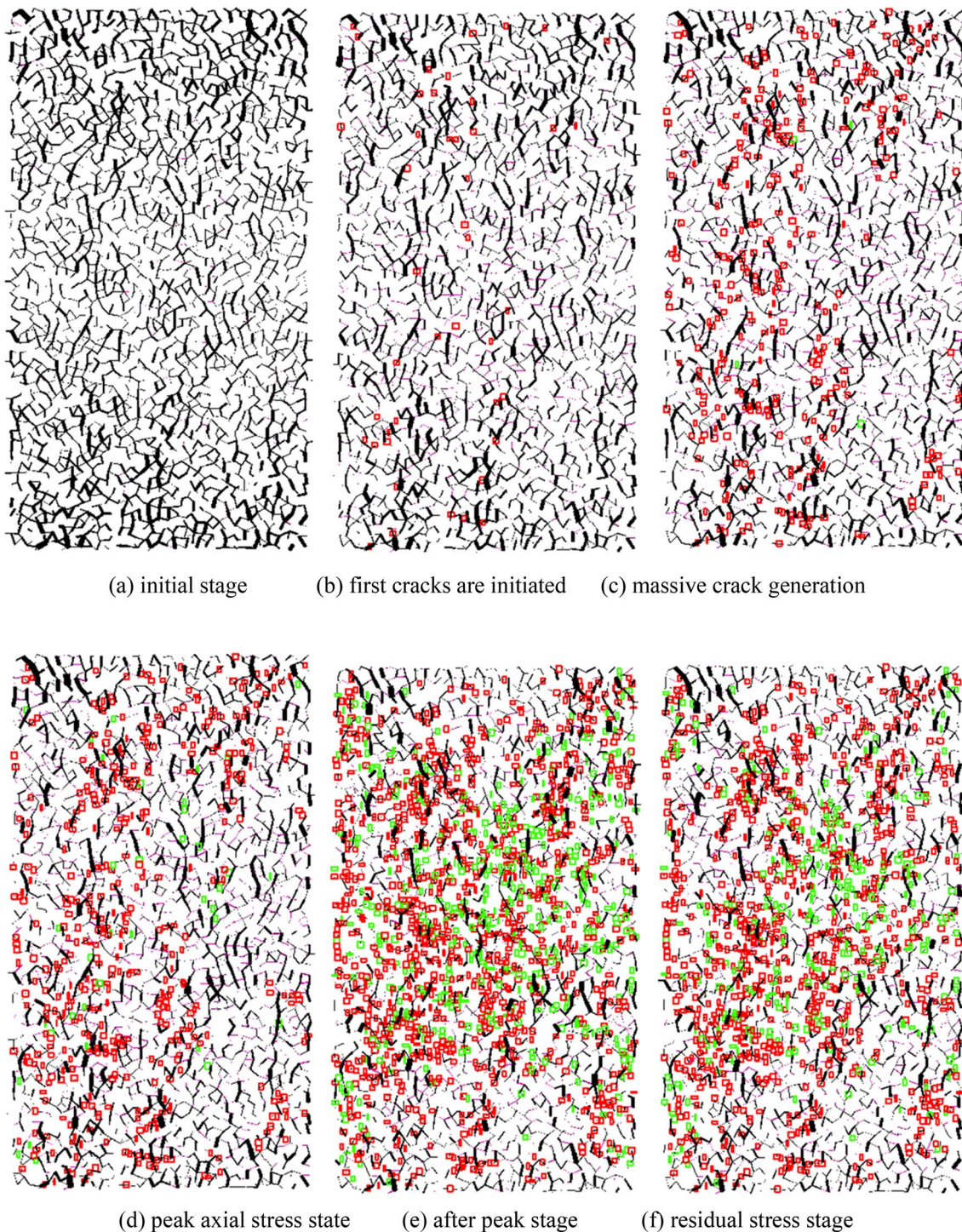
(a) initial stage   (b) first cracks are initiated   (c) massive crack generation

(d) peak axial stress state   (e) after peak stage   (f) residual stress stage
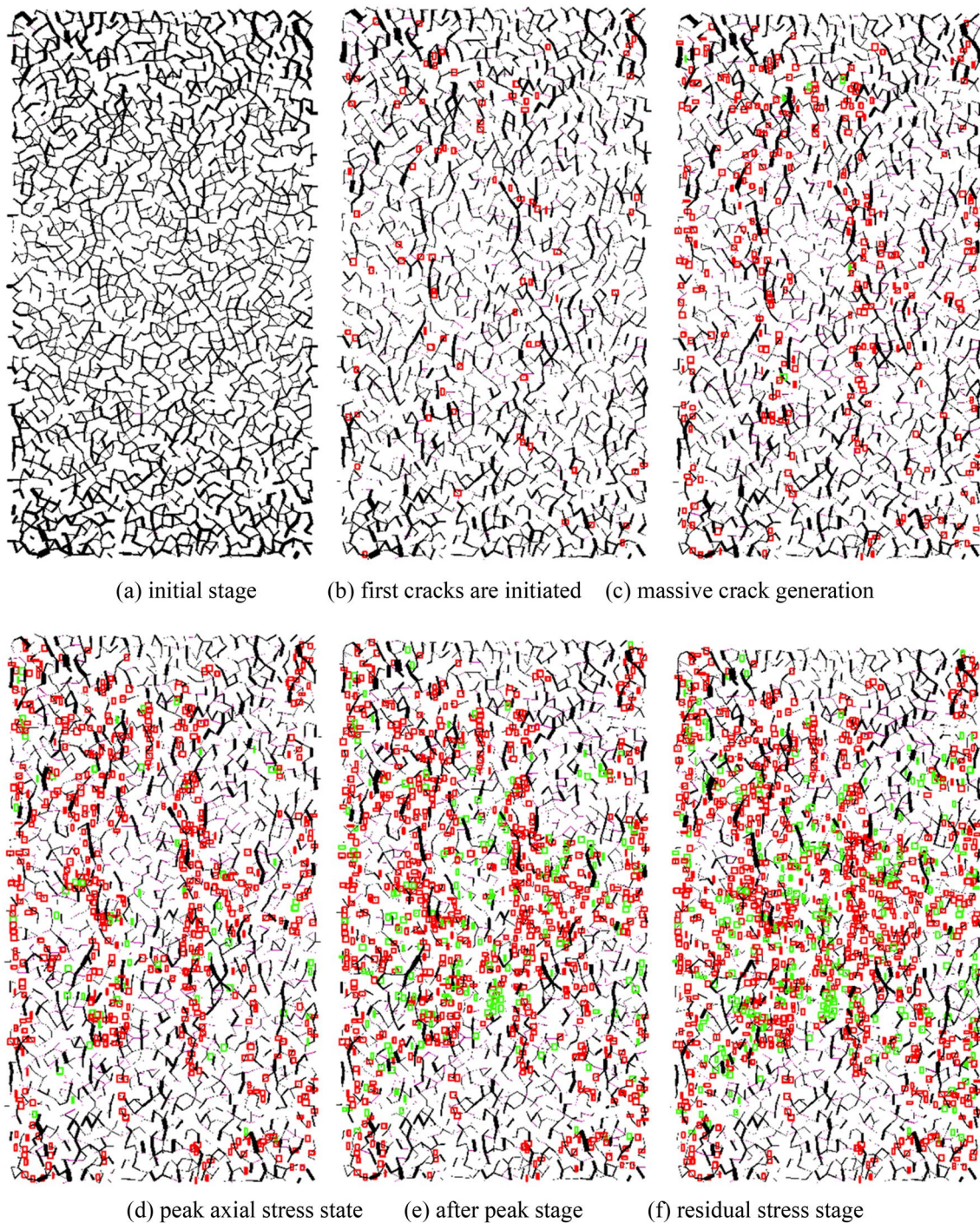
Fig. 18 Contact force chains with cracks for numerical model C1 with 2.5 MPa confining pressure (see Fig. 15) in cross-sectional perspective (shear cracks: red, tensile cracks: green) (Color figure online)

Taking the reconstructed sample model C1 and C4 (see in Fig. 4a, d) under the same confining pressure of 2.5 MPa as examples, the distribution of inclusions inside the coal matrix affecting the damage pattern is shown in Table 8.

The majority of fractures are initiated at the boundary between matrix and inclusions, and propagate along their boundaries. In case of elongated arrangement of inclusions inside the sample the crack path follows the boundary

(a) initial stage   (b) first cracks are initiated   (c) massive crack generation

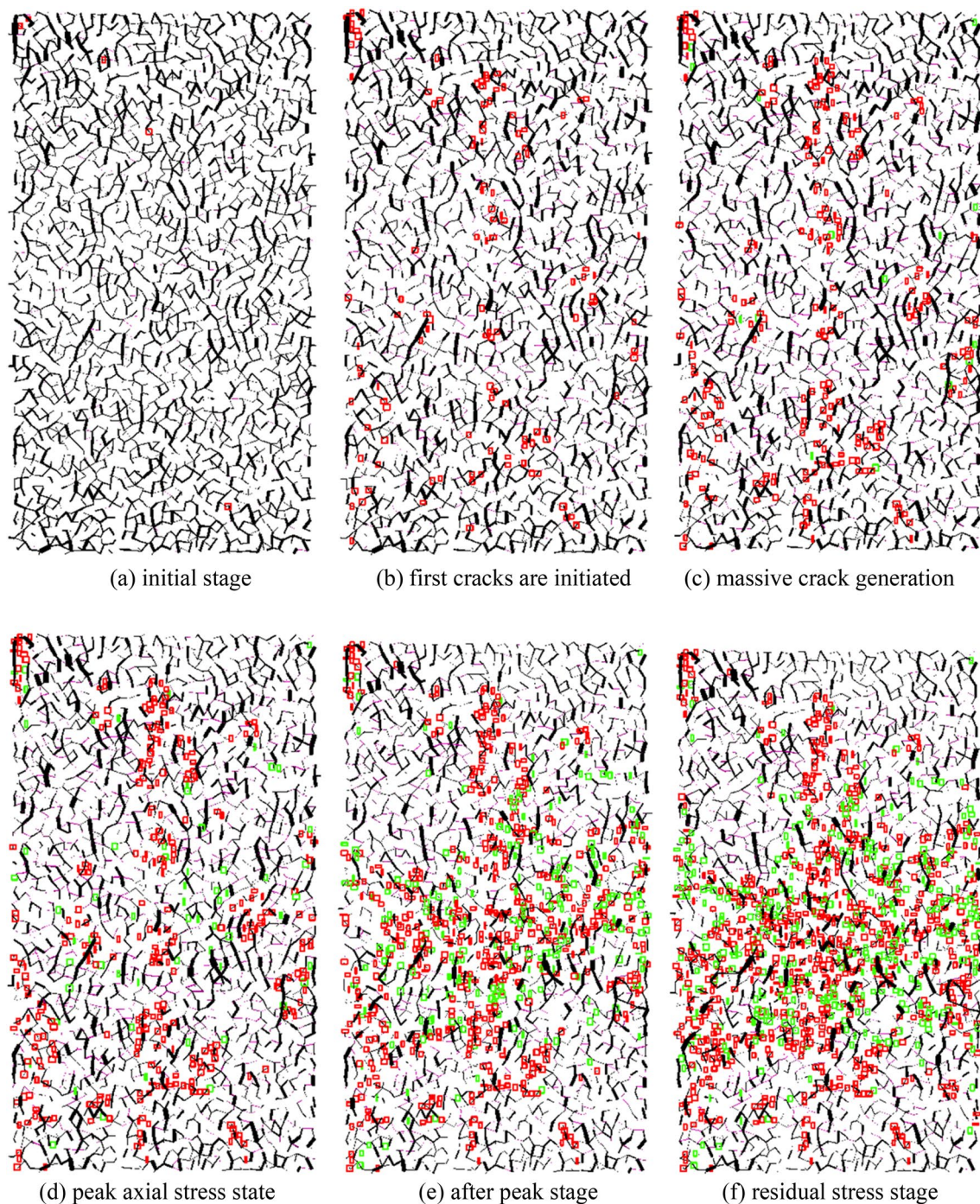(d) peak axial stress state   (e) after peak stage   (f) residual stress stage

Fig. 19 Contact force chains with cracks for numerical model C3 with 5.0 MPa confining pressure (see Fig. 16) in cross-sectional perspective (shear cracks: red, tensile cracks: green) (Color figure online)

between inclusion and matrix. Similar trends are observed in laboratory tests (see Fig. 7).

The peak strength shows strong dependency on confining pressure. Exemplary, the triaxial simulation results for model C1 are shown in Fig. 21 for confining pressures of 2.5, 5.0, and 7.5 MPa (the samples are loaded

initially isotropic until desired confining pressure value is reached). In agreement with the experimental data, higher maximum differential stresses are strongly associated with higher confining pressures. The corresponding strain values at peak stress also increase with higher confining

(a) initial stage   (b) first cracks are initiated   (c) massive crack generation

(d) peak axial stress state   (e) after peak stage   (f) residual stress stage

Fig. 20 Contact force chains with cracks for numerical model C4 with 7.5 MPa confining pressure (see Fig. 17) in cross-sectional perspective (shear cracks: red, tensile cracks: green) (Color figure online)

pressure, similar results are also shown in previous works (e.g. Baumgarten and Konietzky 2013).

Number of induced cracks increase drastically when axial stress reaches about 30% to 40% of the peak value, and increases again slightly at peak stress, which is consistent with previous works (Xue 2007; Stoeckhert et al. 2015). This means: large amount of microcracks are generated long before peak stress is reached, but macroscopic fractures are formed later. In the final state of the simulation, more cracks are generated in models with higher confining pressure. Because the lateral deformation is restrained, instead of generating macroscopic fractures, more microcracks develop inside the sample.

Table 8 Force chains and damage patterns in models C1 and C4 (red: shear failure, green: tensile failure)

Model model	70% of peak stress	At peak stress	Residual stage
C1 (σ_3: 2.5 MPa)			
C4 (σ_3: 2.5 MPa)			
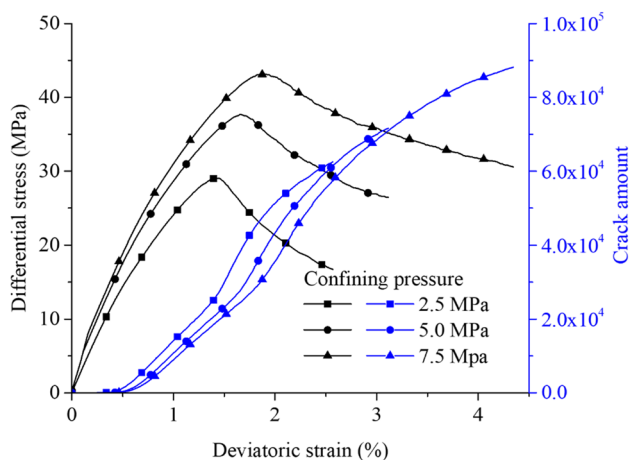
Fig. 21 Differential stress and amount of cracks for model C1 versus axial strain during deviatoric stress regime for different confining pressures

According to the numerical simulations, opening and closure of microcracks influence the mechanical behavior of the damaged model directly. The emerging of microcracks induce displacement jumps along crack surfaces [see also previous works of Kachanov (1982a, b) and Yeo et al. (1998)]. The relative motion of particles and the bonding method with predefined failure criteria controls variation in mechanical behavior of fractures such as opening, closure, sliding and dilation.

7 Conclusions

X-ray CT techniques offer some remarkable advantages such as non-destructive detection and 3D visualization of the inner heterogeneity of the samples. Three structural components were detected inside the coal sample: pores (including fractures), coal matrix, and mineral inclusions. The distribution of the inclusions inside the coal samples is

highly inhomogeneous. Numerical models of coal samples replicating the inner structure are built.

Triaxial compression tests of coal samples with inclusions were conducted in the laboratory. The deformation patterns of the samples are directly related to the fracture connectivity. Fracture aperture, fracture plane evolution and fracture orientation are the main factors to evaluate the degree of damage. By further analyzing both—images and lab test data—it becomes obvious that fractures propagate through the samples easily at low confining pressures. On the contrary, at high confining pressure, only a few main fractures are generated with orientation towards the side surfaces until complete failure of the sample. Peak differential stress of the samples depends heavily on confining pressure.

A novel flexible wall approach has been developed to simulate the triaxial tests with the PM code PFC^{3D}. The flexible wall is composed of triangular wall elements. This approach is validated by comparing the stress–strain response and fracture pattern of coal samples tested in the laboratory. Compared with rigid wall boundary and particle membrane approach, the FW approach shows much better consistency with real samples, because this approach allows large and inhomogeneous lateral deformations. A series of triaxial compression tests with reconstructed numerical models was performed. Microcracks and macroscopic fractures propagate along the boundaries between matrix and inclusions. The obtained stress–strain curve can be directly related to the accumulation of fractures. Force chain development and crack distributions are also affected by the distribution of inclusions inside the sample. A higher proportion of hard minerals (inclusions) leads to higher peak strength.

References

Baumgarten L, Konietzky H (2012) Stress-strain, strength and failure behavior of Postaer Sandstone in tension and compression tests–laboratory investigations and numerical modelling with PFC3D. In: Proc. 41. Geomechanics-Colloquium. Publ. Geotechnical Institute TU Bergakademie, Freiberg, 2012-1, pp 41–61

Baumgarten L, Konietzky H (2013) Investigations on the fracture behaviour of rocks in a triaxial compression test. Proc. ISRM International Symposium-EUROCK 2013. International Society for Rock Mechanics and Rock Engineering, Warsaw, pp 861–866

Belheine N, Plassiard JP, Donzé FV et al (2009) Numerical simulation of drained triaxial test using 3D discrete element modeling. Comput Geotech 36:320–331. https://doi.org/10.1016/j.compgeo.2008.02.003

Cheung G, O'Sullivan C (2008) Effective simulation of flexible lateral boundaries in two- and three-dimensional DEM simulations. Particuology 6:483–500. https://doi.org/10.1016/j.partic.2008.07.018

Cnudde V, Boone MN (2013) High-resolution X-ray computed tomography in geosciences: a review of the current technology and applications. Earth-Sci Rev 123:1–17. https://doi.org/10.1016/j.earscirev.2013.04.003

Cui L, O'Sullivan C, O'Neill S (2008) An analysis of the triaxial apparatus using a mixed boundary three-dimensional discrete element model. Géotechnique 57:831–844. https://doi.org/10.1680/geot.2007.57.10.831

de Bono J, Mcdowell G, Wanatowski D (2013) Discrete element modelling of a flexible membrane for triaxial testing of granular material at high pressures. Géotechnique Lett 2:199–203. https://doi.org/10.1680/geolett.12.00040

Hasan A, Alshibli KA (2010) Discrete element modeling of strength properties of Johnson Space Center (JSC-1A) Lunar Regolith Simulant. J Aerosp Eng 23:157–165. https://doi.org/10.1061/(asce)as.1943-5525.0000020

Itasca (2008) PFC3D-Particle Flow Code in 3 Dimensions, Ver. 3.10–305. Itasca Consulting Group Inc., Minneapolis

Kachanov ML (1982a) A microcrack model of rock inelasticity part I: frictional sliding on microcracks. Mech Mater 1:19–27. https://doi.org/10.1016/0167-6636(82)90021-7

Kachanov ML (1982b) A microcrack model of rock inelasticity part II: propagation of microcracks. Mech Mater 1:29–41. https://doi.org/10.1016/0167-6636(82)90022-9

Karacan CÖ (2009) Reservoir rock properties of coal measure strata of the Lower Monongahela Group, Greene County (Southwestern Pennsylvania), from methane control and production perspectives. Int J Coal Geol 78:47–64. https://doi.org/10.1016/j.coal.2008.10.005

Karacan CÖ, Okandan E (2000) Fracture/cleat analysis of coals from Zonguldak Basin (northwestern Turkey) relative to the potential of coalbed methane production. Int J Coal Geol 44:109–125. https://doi.org/10.1016/S0166-5162(00)00004-5

Karpyn ZT, Alajmi A, Radaelli F et al (2009) X-ray CT and hydraulic evidence for a relationship between fracture conductivity and adjacent matrix porosity. Eng Geol 103:139–145. https://doi.org/10.1016/j.enggeo.2008.06.017

Ketcham RA, Carlson WD (2001) Acquisition, optimization and interpretation of x-ray computed tomographic imagery: applications to the geosciences. Comput Geosci 27:381–400. https://doi.org/10.1016/S0098-3004(00)00116-3

Kuhn M (1995) A flexible boundary for three-dimensional dem particle assemblies. Eng Comput 12:175–183. https://doi.org/10.1108/02644409510799541

Kumar H, Lester E, Kingman S et al (2011) Inducing fractures and increasing cleat apertures in a bituminous coal under isotropic stress via application of microwave energy. Int J Coal Geol 88:75–82. https://doi.org/10.1016/j.coal.2011.07.007

Lu Y, Frost D (2010) Three-dimensional DEM modeling of triaxial compression of sands. In: Geoshanghai International Conference. Shanghai, pp 220–226

Mahabadi OK, Randall NX, Zong Z, Grasselli G (2012) A novel approach for micro-scale characterization and modeling of geomaterials incorporating actual material heterogeneity. Geophys Res Lett 39:L01303. https://doi.org/10.1029/2011GL050411

Mazumder S, Wolf K-HAA, Elewaut K, Ephraim R (2006) Application of X-ray computed tomography for analyzing cleat spacing and cleat aperture in coal samples. Int J Coal Geol 68:205–222. https://doi.org/10.1016/j.coal.2006.02.005

National Bureau of Statistics of China (2018) China statistical yearbook. CSS Bureau, Beijing

O'Sullivan C, Cui L (2009) Micromechanics of granular material response during load reversals: combined DEM and experimental study. Powder Technol 193:289–302. https://doi.org/10.1016/j.powtec.2009.03.003

Polak A, Elsworth D, Yasuhara H et al (2003) Permeability reduction of a natural fracture under net dissolution by hydrothermal fluids. Geophys Res Lett 30:1–4. https://doi.org/10.1029/2003GL017575

Potyondy DO, Cundall PA (2004) A bonded-particle model for rock. Int J Rock Mech Min Sci 41:1329–1364. https://doi.org/10.1016/j.ijrmms.2004.09.011

Pyrak-Nolte LJ, Montemagno CD, Nolte DD (1997) Volumetric imaging of aperture distributions in connected fracture networks. Geophys Res Lett 24:2343–2346. https://doi.org/10.1029/97GL02057

Randall NX, Vandamme M, Ulm FJ (2009) Nanoindentation analysis as a two-dimensional tool for mapping the mechanical properties of complex surfaces. J Mater Res 24:679–690. https://doi.org/10.1557/jmr.2009.0149

Rédei GP (2008) Encyclopedia of genetics, genomics, proteomics and informatics, 3rd edn. Springer Science & Business Media, New York

Salot C, Gotteland P, Villard P (2009) Influence of relative density on granular materials behavior: DEM simulations of triaxial tests. Granul Matter 11:221–236. https://doi.org/10.1007/s10035-009-0138-2

Simons FJ, Verhelst FF, Swennen R (1997) Quantitative characterization of coal by means of microfocal X-ray computed microtomography (CMT) and color image analysis. Int J Coal Geol 34:69–88. https://doi.org/10.1016/S0166-5162(97)00011-6

Sitharam TG, Dinesh SV, Shimizu N (2002) Micromechanical modelling of monotonic drained and undrained shear behaviour of granular media using three-dimensional DEM. Int J Numer Anal Methods Geomech 26:1167–1189. https://doi.org/10.1002/nag.240

Solomon C, Breckon T (2011) Fundamentals of digital image processing: a practical approach with examples in Matlab. Wiley, New Jersey

Stoeckhert F, Molenda M, Brenne S, Alber M (2015) Fracture propagation in sandstone and slate—laboratory experiments, acoustic emissions and fracture mechanics. J Rock Mech Geotech Eng 7:237–249. https://doi.org/10.1016/j.jrmge.2015.03.011

Ulusay R, Hudson JA (2012) Suggested methods for rock failure criteria: general introduction. Rock Mech Rock Eng 45:971. https://doi.org/10.1007/s00603-012-0273-7

Uthus L, Hopkins MA, Horvli I (2008) Discrete element modelling of the resilient behaviour of unbound granular aggregates. Int J Pavement Eng 9:387–395. https://doi.org/10.1080/10298430802169382

Van Geet M, Swennen R, Wevers M (2001) Towards 3-D petrography: application of microfocus computer tomography in geological science. Comput Geosci 27:1091–1099. https://doi.org/10.1016/S0098-3004(00)00154-0

Verhelst F, David P, Fermont W et al (1996) Correlation of 3D-computerized tomographic scans and 2D-colour image analysis of Westphalian coal by means of multivariate statistics. Int J Coal Geol 29:1–21. https://doi.org/10.1016/0166-5162(95)00026-7

Wang Y, Tonon F (2009) Modeling triaxial test on intact rock using discrete element method with membrane boundary. J Eng Mech 135:1029–1037. https://doi.org/10.1061/(asce)em.1943-7889.0000017

Wolf K-HAA, Ephraim R, Siemons N, Bossie Codreanu D (2004) Analysing cleat angles in coal seams using image analysis techniques on artificial drilling cuttings and prepared coal blocks. Geol Belgica 7:105–113

Wolf K-HAA, van Bergen F, Ephraim R, Pagnier H (2008) Determination of the cleat angle distribution of the RECOPOL coal seams, using CT-scans and image analysis on drilling cuttings and coal blocks. Int J Coal Geol 73:259–272. https://doi.org/10.1016/j.coal.2007.06.001

Xue L (2007) Damage accumulation and fracture initiation in uncracked ductile solids subject to triaxial loading. Int J Solids Struct 44:5163–5181. https://doi.org/10.1016/j.ijsolstr.2006.12.026

Yan Y, Ji S (2010) Discrete element modeling of direct shear tests for a granular material. Int J Numer Anal Methods Geomech 34:978–990. https://doi.org/10.1002/nag.848

Yao Y, Liu D, Che Y et al (2009) Non-destructive characterization of coal samples from China using microfocus X-ray computed tomography. Int J Coal Geol 80:113–123. https://doi.org/10.1016/j.coal.2009.08.001

Yeo IW, De Freitas MH, Zimmerman RW (1998) Effect of shear displacement on the aperture and permeability of a rock fracture. Int J Rock Mech Min Sci 35:1051–1070. https://doi.org/10.1016/S0148-9062(98)00165-X

Zhao X, Evans TM, Asce AM (2009) Discrete simulations of laboratory loading conditions. Int J Geomech 9:169–178. https://doi.org/10.1061/(ASCE)1532-3641(2009)9:4(169)

Zhao Y, Liu S, Zhao G-F et al (2010) Failure mechanisms in coal: dependence on strain rate and microstructure. J Geophys Res Solid Earth Res. https://doi.org/10.1002/2014JB011198

Zhu WC, Liu J, Elsworth D et al (2007) Tracer transport in a fractured chalk: X-ray CT characterization and digital-image-based (DIB) simulation. Transp Porous Media 70:25–42. https://doi.org/10.1007/s11242-006-9080-5